



# Charge transfer and spin-valley locking in 4Hb-TaS<sub>2</sub>



Avior Almoalem<sup>1</sup>, Roni Gofman<sup>1</sup>, Yuval Nitzav<sup>1</sup>, Ilay Mangel<sup>1</sup>, Irena Feldman<sup>1</sup>, Jahyun Koo<sup>2</sup>, Federico Mazzola<sup>3</sup>, Jun Fujii<sup>3</sup>, Ivana Vobornik<sup>3</sup>, J. S'anchez-Barriga<sup>4,5</sup>, Oliver J. Clark<sup>4</sup>, Nicholas Clark Plumb<sup>6</sup>, Ming Shi<sup>6</sup>, Binghai Yan<sup>2</sup> & Amit Kanigel<sup>1</sup> ✉

4Hb-TaS<sub>2</sub> is a superconductor that exhibits unique characteristics such as time-reversal symmetry breaking, hidden magnetic memory, and topological edge modes. It is a naturally occurring heterostructure comprising of alternating layers of 1H-TaS<sub>2</sub> and 1T-TaS<sub>2</sub>. The former is a well-known superconductor, while the latter is a correlated insulator with a possible non-trivial magnetic ground state. In this study, we use angle resolved photoemission spectroscopy to investigate the normal state electronic structure of this unconventional superconductor. Our findings reveal that the band structure of 4Hb-TaS<sub>2</sub> fundamentally differs from that of its constituent materials. Specifically, we observe a significant charge transfer from the 1T layers to the 1H layers that drives the 1T layers away from half-filling. In addition, we find a substantial reduction in inter-layer coupling in 4Hb-TaS<sub>2</sub> compared to the coupling in 2H-TaS<sub>2</sub> that results in a pronounced spin-valley locking within 4Hb-TaS<sub>2</sub>.

Over the past few years, the field of quantum condensed matter research has undergone a significant revolution, thanks to breakthroughs in stacking atomically thin materials with diverse properties and at arbitrary relative angles<sup>1</sup>.

These heterostructures exhibit a variety of interacting phases, including superconductivity (SC)<sup>2</sup>, correlated insulators<sup>3</sup>, structural and electronic ferroelectrics<sup>4</sup>, electronic nematicity<sup>5</sup>, and magnetism<sup>6</sup>.

Alternate stacking structures of TaS<sub>2</sub> have also drawn significant attention. The natural occurring heterostructure, 4Hb-TaS<sub>2</sub>, formed by alternate stacking of 1T-TaS<sub>2</sub> and 1H-TaS<sub>2</sub><sup>7–10</sup> is a superconductor with unusual properties that led some of us to propose that it is a chiral superconductor<sup>9–12</sup>. In contrast, bi-layers made by growing mono-layers of 1T-TaS<sub>2</sub> and 1H-TaS<sub>2</sub>, are not superconducting and instead show Kondo physics<sup>13</sup> or doped Mott physics<sup>14</sup>.

The charge density wave (CDW) reconstruction in 1T-TaS<sub>2</sub> results in a state consisting of a super-lattice, where every 13 atoms form a star-of-David cell with one localized electron. In bulk 1T-TaS<sub>2</sub> this leads to a Mott transition and possibly to a quantum spin liquid<sup>8,15</sup>.

These localized states are believed to play a crucial role both in 4Hb-TaS<sub>2</sub> and in the bi-layers. In 4Hb-TaS<sub>2</sub>, it was suggested that the proximity of the strongly correlated 1T layers to the superconducting 1H layers is responsible for the observed time-reversal symmetry breaking<sup>11,16,17</sup>. In the

artificial bi-layers, the localized moments on the 1T layers are Kondo screened by the itinerant electrons in the 1H layers<sup>13</sup>.

A remaining open question is how the proximity between the 1T and the 1H layers alters their properties, specifically, the extent to which the Mott physics, believed to govern the physics of 1T-TaS<sub>2</sub> plays a role in 4Hb-TaS<sub>2</sub>. In this paper, we address this question using angle resolved photoemission spectroscopy (ARPES), comparing in detail the electronic structure of 2H-TaS<sub>2</sub> and 4Hb-TaS<sub>2</sub>.

## Results

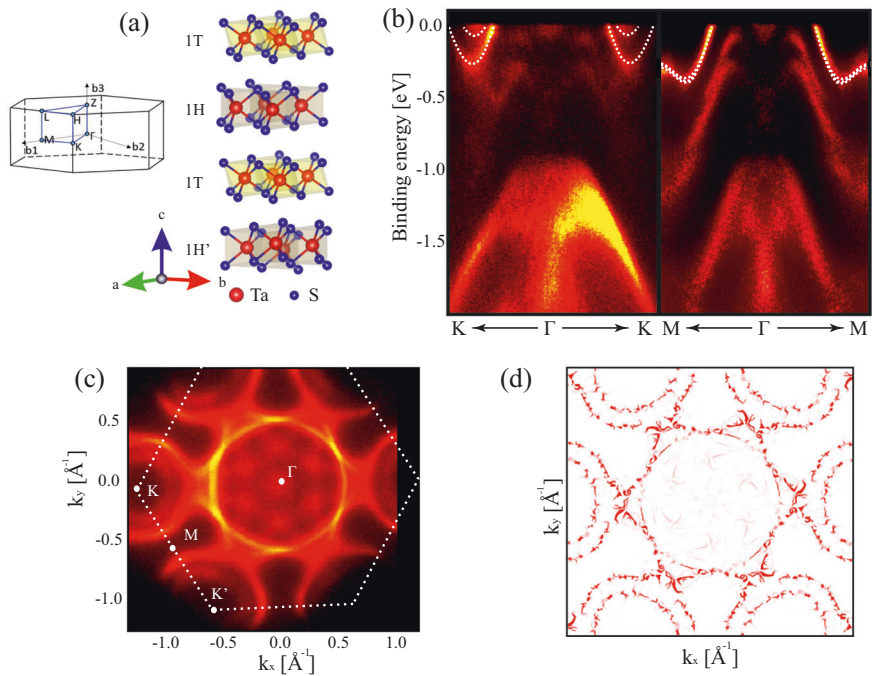
### Charge transfer in 4Hb-TaS<sub>2</sub>

Both 4Hb and 2H polymorphs of TaS<sub>2</sub> belong to the P6<sub>3</sub>/mmc hexagonal space group, the unit cell of 4Hb-TaS<sub>2</sub> is shown in Fig. 1a. 4Hb-TaS<sub>2</sub> undergoes a CDW transition at  $T = 315$  K and a sharp SC transition at  $T_c = 2.7$  K<sup>7,11,18</sup>, while 2H-TaS<sub>2</sub> has a CDW transition at 75 K and  $T_c$  of 0.8 K<sup>7</sup>. Most of the intensity at the Fermi level in both 2H and 4Hb is from the Ta atoms in 1H layers which have a non-centrosymmetric structure<sup>7</sup>. Both polymorphs contain two 1H layers stacked with a relative 180° rotation in-plane, resulting in an overall inversion-symmetric structure<sup>11,19</sup>.

ARPES spectra along the high symmetry lines of 4Hb-TaS<sub>2</sub>,  $\Gamma$ -K and  $\Gamma$ -M, are shown in Fig. 1b. Similar data from 2H-TaS<sub>2</sub> is shown in Supplementary Fig. 1. Comparing the ARPES data for both polymorphs reveals

<sup>1</sup>Physics Department, Technion-Israel Institute of Technology, Haifa 32000, Israel. <sup>2</sup>Department of Condensed Matter Physics, Weizmann Institute of Science, Rehovot 7610001, Israel. <sup>3</sup>Istituto Officina dei Materiali (IOM)-CNR, Area Science Park, S.S.14, Km 163.5, 34149 Trieste, Italy. <sup>4</sup>Helmholtz-Zentrum Berlin für Materialien und Energie, BESSY II, Albert-Einstein-Strasse 15, 12489 Berlin, Germany. <sup>5</sup>IMDEA Nanoscience, C. Faraday, 9, Fuencarral-El Pardo, 28049 Madrid, Spain. <sup>6</sup>Photon Science Division, Paul Scherrer Institute, CH-5232 Villigen PSI, Switzerland. ✉e-mail: [amitk@physics.technion.ac.il](mailto:amitk@physics.technion.ac.il)

**Fig. 1 | Band Structure and Fermi surface of 4Hb-TaS<sub>2</sub>.** **a** The unit cell of 4Hb-TaS<sub>2</sub> with the 1T and 1H layers. The 1H and 1H' layers are rotated by 180° degrees. Brillouin zone of the 3D crystal structure showing the high symmetry points. **b**<sub>1</sub>, **b**<sub>2</sub> and **b**<sub>3</sub> are reciprocal lattice vectors. **b** ARPES spectra taken with  $\hbar\nu = 102$  eV. The spectra are taken along high symmetry lines of the Brillouin zone. Dashed lines are DFT calculations of the 1H-layers derived bands in 4Hb-TaS<sub>2</sub>, done on a slab of 10 unit cells. Other bands are different from bands in the bulk 2H and 1T polymorphs<sup>20</sup>. Shallow electron pockets are visible at the  $\Gamma$  point matching qualitatively the DFT results. **c** Fermi-surface of 4Hb-TaS<sub>2</sub>. The data is in good agreement with the DFT results. The 2D hexagonal Brillouin zone is shown with white dashed lines. **d** Fermi surface from a DFT calculation on a 1T/1H bi-layer. The 1T CDW ( $\sqrt{13} \times \sqrt{13}$ ) was included in calculations and the Fermi surface was unfolded to the original Brillouin zone for comparison with experiments. The small Fermi pockets produced by the shallow bands are clearly seen.



that the bands derived from the 1H layers are similar in both structures but not identical.

The inner pocket along the K-M-K' line, derived from the 1H layer, is  $\sim 100$  meV deeper compared to 2H-TaS<sub>2</sub>. Additionally, there are other bands originating from the 1T layers, these bands are notably different from the bands in bulk 1T-TaS<sub>2</sub><sup>20</sup>. In particular, there are several shallow pockets with Fermi energies of about 50 meV around the  $\Gamma$  point.

The measured Fermi-surface is shown in Fig. 1c, and the Fermi-surface calculated using density-functional theory (DFT) is shown in Fig. 1d. The agreement between the DFT and the ARPES data is remarkable. The new bands form a rather complicated set of small pockets around  $\Gamma$  that seem to have a chiral structure, reminiscent of the chirality found in the charge density wave (CDW) in bulk 1T-TaS<sub>2</sub><sup>21</sup>. The ARPES data is in agreement with the STM data from the same sample<sup>22</sup>, which identifies a band located just above the Fermi level with only a weak density of states crossing the Fermi level. The role of these new bands in superconductivity is not clear. It has been suggested that Kondo physics seen in 4Hb<sup>22,23</sup> and in 1T/1H bi-layers<sup>13</sup> could be related to these narrow bands.

Other bands along the  $\Gamma$ -K line, suggested to originate from the 1T layer by DFT, are similar to bands in bulk 1T-TaS<sub>2</sub>.

DFT finds a significant charge transfer from the 1T to the 1H layers. The charge transfer depends strongly on the inter-layer distance<sup>14</sup>. For a spacing of 5.9 Å it is found that the entire localized electron on the star-of-David cluster is transferred to the 1H layers<sup>9</sup>.

The ARPES data show clear evidence of charge transfer. First, the pocket along the K-M-K' line is deeper in 4Hb-TaS<sub>2</sub> by about 100 meV compared to 2H-TaS<sub>2</sub> (Supplementary Figs. 2 and 3). The agreement between the DFT and the ARPES data further supports the observation of the charge transfer. To directly measure the charge transfer, we compare the Fermi-surface area of 4Hb-TaS<sub>2</sub> and 2H-TaS<sub>2</sub> in Fig. 2. We find that the hole pocket around  $\Gamma$  of 4Hb-TaS<sub>2</sub> is smaller than in 2H-TaS<sub>2</sub>, while the “dog-bone”-shaped electron pocket is larger.

Quantitatively, by integrating the differences between the Fermi-surface areas, we estimate the total charge transfer to be  $0.071 \pm 0.008$  electron per Ta atom, or  $0.92 \pm 0.11$  per star-of-David. It is worth noting that this estimate ignores the contribution of the new small pockets around  $\Gamma$ , but these seem to enclose a very small area. Nevertheless, the fact that these shallow bands do produce Fermi-pockets, suggests that although the charge transfer is significant the depletion of the 1T flat band is not

complete. For the details of the charge transfer estimate, see Supplementary Note 3.

Next, we estimate the effect of the 1T alternate stacking on the coupling between the 1H layers. A comparison between 2H-TaS<sub>2</sub> and 4Hb-TaS<sub>2</sub> reveals a completely different behavior. In Fig. 3a, c, we present ARPES data measured along the K-M-K' line ( $k_z = 0$ ) for 2H-TaS<sub>2</sub> and 4Hb-TaS<sub>2</sub>, respectively. The black lines represent the DFT calculated dispersion. The gap between the inner and outer pockets at the M point in 2H-TaS<sub>2</sub> is result of the inter-layer coupling between the 1H layers. In contrast, no gap is observed at the M-point in the 4Hb-TaS<sub>2</sub> spectra, similar to the monolayer case<sup>24</sup>. The connection between the gap at the M-point and the inter-layer coupling was already pointed out<sup>25,26</sup>.

The 1H monolayer exhibits an Ising spin texture due to the  $M_z$  mirror symmetry. We use a simple effective model that includes two Ising layers to extract the inter-layer interaction from the data:

$$H = \frac{\hbar^2}{2m^*} \sigma_0 \tau_0 k^2 + \alpha \sigma_z \tau_z k + \sigma_0 \tau_x t \quad (1)$$

where  $\sigma$  are the Pauli matrices for the spin and  $\tau$  are the Pauli matrices representing the layer,  $\alpha$  is the spin-orbit coupling (SOC) and  $t$  is the inter-layer coupling (ILC). The best fit to the data (Supplementary Fig. 4) yields an inter-layer coupling of  $65 \pm 5$  meV in 2H-TaS<sub>2</sub> and a vanishing inter-layer coupling in 4Hb-TaS<sub>2</sub> within our resolution. The Ising spin-orbit coupling was set to be equal in both materials and is estimated to be  $680 \pm 40$  meVÅ. Our results for 2H-TaS<sub>2</sub> agrees with previously measured values<sup>27</sup>.

Energy-distribution curves (EDCs) at different  $k_z$  values were measured by varying the photon energy (Supplementary Fig. 5). The EDCs along the M-L line for both polymorphs are shown in Fig. 3b, d. In 2H-TaS<sub>2</sub> (Fig. 3b), we observe a significant dispersion with a bandwidth of about 150 meV. The band split, created by the inter-layer coupling, is maximal at the M-point and it vanishes at the L-point due to a glide-mirror symmetry that prevents the lift of the degeneracy<sup>28,29</sup>.

In 4Hb-TaS<sub>2</sub> (Fig. 3d), on the other hand, there is no dispersion at all, suggesting the inter-layer coupling is negligible. We found no  $k_z$  dependence in the width of the EDCs either, indicating that there is no measurable gap at any  $k_z$  point, as expected from a 2D system.

The 2D character of 4Hb-TaS<sub>2</sub> can also explain the sharpness of the ARPES spectra at the Fermi-level compared to the data of 2H-TaS<sub>2</sub>. In a

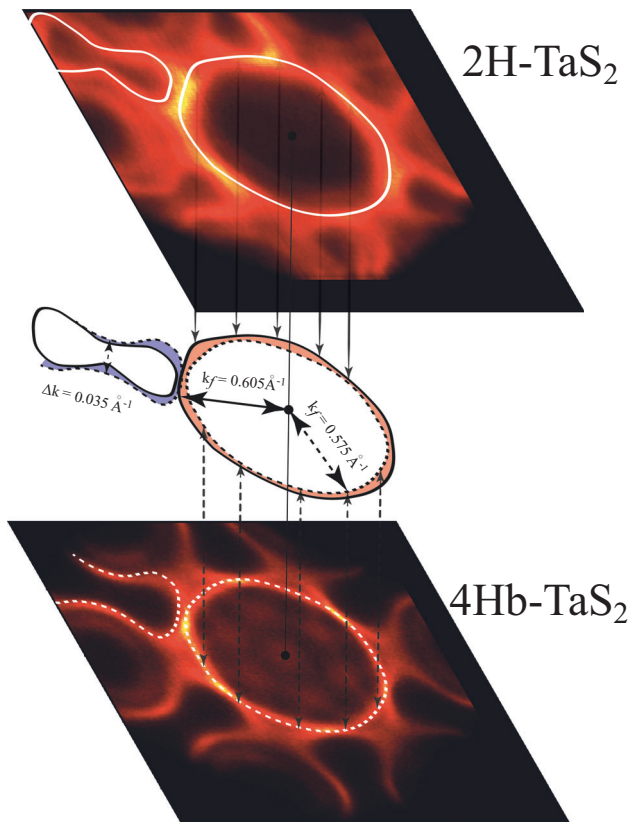


**Fig. 2 | Charge transfer in 4Hb-TaS<sub>2</sub>.** Fermi surface contours extracted from ARPES spectra of 2H-TaS<sub>2</sub> (upper panel) and 4Hb-TaS<sub>2</sub> (lower panel) overlapped. The dashed lines correspond to 4Hb-TaS<sub>2</sub>, and the solid lines correspond to 2H-TaS<sub>2</sub>, the lines were drawn by following the maximum intensity at the Fermi level. In the middle panel, red filling shows the contracting hole pocket around the  $\Gamma$  point, and the blue filling shows the expanding “dog-bone” electron pockets, around the M point.  $k_F$  measured from the M-point in the narrow part “dog-bone” is  $0.323 \text{ \AA}^{-1}$  and  $0.358 \text{ \AA}^{-1}$  for 2H-TaS<sub>2</sub>, and 4Hb-TaS<sub>2</sub>, respectively. The change in  $k_F$  of the K-point pocket is too small to show in the figure. The estimated errors in  $k_F$  of the hole pocket and the “dog-bone” are  $0.008 \text{ \AA}^{-1}$  and  $0.005 \text{ \AA}^{-1}$ , respectively. Overall, the differences agrees with the DFT results of the 1H/1T bi-layer. Data for both samples was measured close to  $k_z = 0$  (92 eV for 2H-TaS<sub>2</sub> and 102 eV for 4Hb-TaS<sub>2</sub>).

three-dimensional system, the finite  $k_z$  resolution results in a broadening of the spectra.

At the Brillouin zone edge, it seems that the main role of the 1T layers is to reduce the inter-layer coupling. The effective mass of the valleys, estimated using our model, is  $m^* = 0.78 \pm 0.05 m_e$  in both 4Hb-TaS<sub>2</sub> and 2H-TaS<sub>2</sub>. This suggests that the 1T layer mainly affects the band dispersion around the  $\Gamma$  point. This is due to the in-plane nature of the orbitals forming the bands at the M and K points, which are  $d_{xy}$  and  $d_{x^2-y^2}$ <sup>9,30</sup>. This is opposed to the orbitals at the  $\Gamma$  point,  $d_{z^2}$ <sup>22,31</sup>, where hybridization between states of 1H and 1T layers takes place. The negligible inter-layer coupling between the 1H layers in 4Hb-TaS<sub>2</sub> suggests a picture in which the electronic states are localized on individual 1H layers<sup>25,28,32–37</sup>. The combination of a large spin-orbit coupling with the non-centrosymmetric structure of the 1H layers is expected to result in a strong spin-valley locking in 1H-derived bands<sup>28,32–34</sup> (Supplementary Fig. 6).

### Spin-valley locking in 4Hb-TaS<sub>2</sub>

We use spin-resolved ARPES to directly measure the spin texture of the electronic bands and the Fermi-surface. First, we focus on the spin polarization at the Fermi-level. In Fig. 4a, we present an ARPES intensity map of part of the Fermi-surface. One can observe the characteristic “dog-bone” shaped Fermi-pockets and the two electron pockets centered around K and

K'. In the inset, we show the DFT calculated spin-resolved Fermi-surface. DFT finds perfect spin-valley locking, meaning that the electron pockets around K and K' have opposite polarization and the electron-spin polarization on the “dog-bone” changes on crossing the  $\Gamma$ -M line. In Fig. 4b, we show the spin-resolved MDCs measured along the dashed line in Fig. 4a (for a full spin-map see Supplementary Fig. 7). The spin is measured normal to the plane, where the red and blue curves represent spin-up and spin-down, respectively. The measured cut in momentum space crosses the Fermi-surface 4 times. From the MDCs it is clear that the polarization changes sign four times on each  $k_F$  crossing. In Fig. 4c, we show the spin polarization out of plane, defined as:  $P = \frac{I_{\uparrow} - I_{\downarrow}}{I_{\uparrow} + I_{\downarrow}}$ , where S, is the Sherman function. We find a polarization of up to 85%, in good agreement with the DFT results. A measurement along a similar momentum cut in 2H-TaS<sub>2</sub> shows no polarization. The MDCs cross the same 4 bands (Fig. 4e), but the polarization shown in Fig. 4f, is negligible.

Next, we compare the polarization at different binding energies. ARPES spectra along the M-K line is shown in Fig. 5a, d for 4Hb-TaS<sub>2</sub> and 2H-TaS<sub>2</sub>, respectively. ARPES data were measured using 55 eV photons. In Fig. 5b, e, we present spin-resolved EDCs measured in the momentum range marked by white lines in Fig. 5a, d. The out-of-plane spin polarization is presented in Fig. 5c, f. The same picture emerges; we find significant polarization in 4Hb-TaS<sub>2</sub>, while no polarization is found in 2H-TaS<sub>2</sub>. Additionally, we find that the polarization in 4Hb-TaS<sub>2</sub> is larger for low binding energies and decreases at high binding energies.

### Discussion

We find that the presence of 1T layers between 2H layers has two main effects: (1) About 1 electron per star-of-David is transferred to the 1H layers, and (2) the 1T layers suppress the coupling between the 1H layers.

The charge transfer leads to an almost complete depletion of the 1T layers and it seems to rule out any Mott-like physics in 4Hb-TaS<sub>2</sub>, which is believed to be important in bulk 1T-TaS<sub>2</sub><sup>15,38</sup>. Saying that, we note that we do find new small electron pockets around the  $\Gamma$ -point. Using STM, Kondo peaks were found in about 10% of the Star-of-David sites, indicating that the charge from these sites was not transferred to the 1H layers<sup>22</sup>. It is possible that these sites are the origin of the small pockets we observe.

Based on the ARPES data, it appears that there are almost no localized moments in the 1T layers, making it is difficult to understand how the remaining dilute charges in the 1T layers can account for the unconventional magnetism observed in the superconducting state of 4Hb-TaS<sub>2</sub><sup>10,16</sup>, nor for the breaking of time-reversal symmetry<sup>11</sup>.

The diminishing inter-layer coupling has far reaching consequences. It suggests that 4Hb-TaS<sub>2</sub> can be thought of as a stack of 2D 1H superconducting layers separated by 1T layers. This can explain the increase in  $T_c$ . It is known that in 2H-TaS<sub>2</sub>  $T_c$  increases as the samples become thinner,  $T_c$  in the limit of a monolayer is similar to the  $T_c$  of 4Hb-TaS<sub>2</sub><sup>26</sup>.

The absence of inter-layer coupling, combined with the strong spin-orbit coupling, naturally explains the Ising-superconductor behavior, as evident in the large anisotropy of  $H_{c2}$  in 4Hb-TaS<sub>2</sub><sup>11</sup>. The strong pinning of the spin out-of-plane results in an in-plane critical field exceeding the Clogston-Chandrasekhar limit by a factor of 5.

Both 4Hb-TaS<sub>2</sub> and 2H-TaS<sub>2</sub> have an overall inversion symmetric-structure; nevertheless, we do observe strong valley-dependent polarization in 4Hb-TaS<sub>2</sub>. Each 1H layer is non-centrosymmetric and does allow for spin-valley locking. Overall, the bands should be doubly degenerate and the spin-valley locking of each 1H layer should cancel with the contribution from the 180 deg rotated 1H' layer. However, since ARPES is a very surface-sensitive probe, it mainly probes the top-most 1H layer and the electrons from deeper layers will not cancel the net polarization.

The level of polarization ARPES should detect depends mainly on how localized are the wave functions on the individual non-centrosymmetric 1H layers. A simple argument shows that the level of polarization of an individual layer is set by  $P \propto \frac{1}{\sqrt{1+(t/\lambda_{soc})^2}}$  where t and  $\lambda_{soc}$  are the inter-layer coupling and spin-orbit coupling parameters, respectively<sup>32</sup>. Large inter-



**Fig. 3 | Inter-layer coupling.** **a, c** ARPES data along the K-M-K' line for 2H-TaS<sub>2</sub> and 4Hb-TaS<sub>2</sub>, respectively. The solid lines are calculated surface bands from a 4Hb slab model. In 2H-TaS<sub>2</sub> there is a clear gap at the M-point which is a result of a significant inter-layer coupling. In 4Hb-TaS<sub>2</sub> we find no gap in the ARPES data within our resolution (about 5 meV), suggesting that the 1H layers are very weakly coupled. The 2D nature of 4Hb-TaS<sub>2</sub> is also evident in the  $k_z$  dispersion. **b, d** We show the dispersion along the M-L line for 2H-TaS<sub>2</sub> and 4Hb-TaS<sub>2</sub>. The dispersion normal to the plane is measured by scanning the photon energy. In 2H-TaS<sub>2</sub> we find a bandwidth of about 150 meV. The inter-layer coupling is maximal at the M-point and vanishes at the L-point. In 4Hb-TaS<sub>2</sub>, on the other hand, we find a completely flat band normal to planes, as expected from a purely 2D system. Arrows mark the energy of the bands at each  $k_z$ , and were obtained by fitting the EDCs to two Lorentzian functions. For 2H-TaS<sub>2</sub> we measured with photon energies between 46eV and 82 eV, and for 4Hb-TaS<sub>2</sub> with photon energies between 49 and 66 eV.

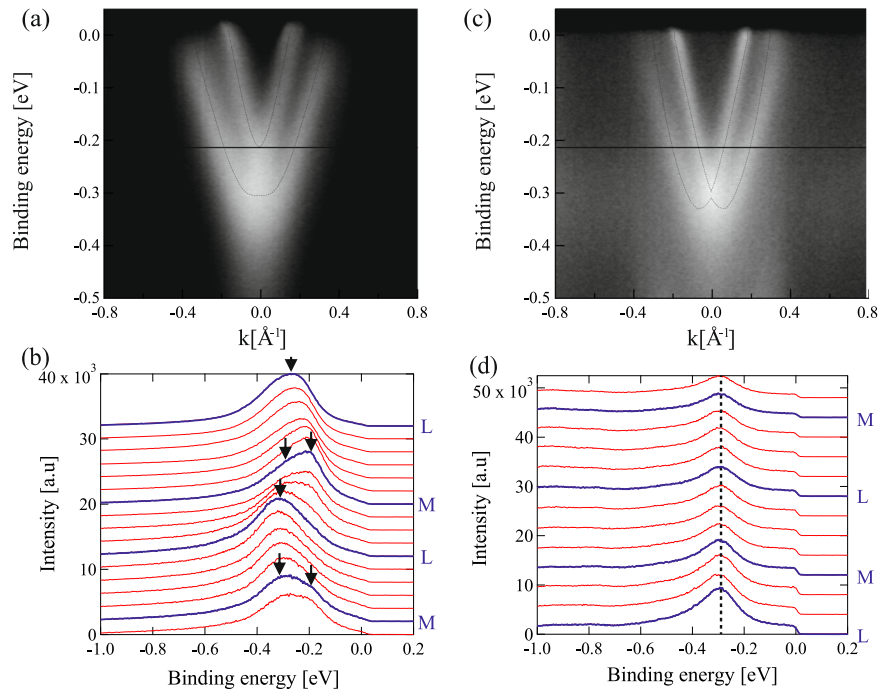
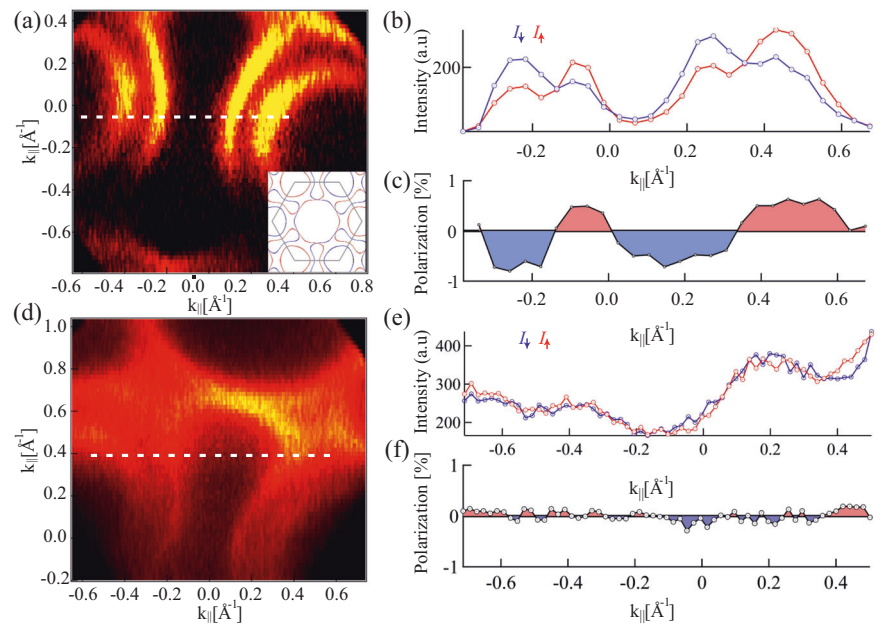


**Fig. 4 | Spin-valley locking.** **a, d** A portion of the Fermi-surface of 4Hb-TaS<sub>2</sub> (**a**) and 2H-TaS<sub>2</sub> (**d**) measured using  $h\nu = 25$  eV photons. The photon energy is optimized for maximum intensity of the polarized bands. The white dashed lines represents the momentum cut for which the spin-resolved MDCs were measured. In both ARPES maps the (0,0) point was chosen to be the M point. Inset: DFT calculations of the spin-polarized states derived from the 1H layer. **b** Spin-polarized MDCs of 4Hb-TaS<sub>2</sub> measured at the Fermi-level along the dashed line shown in (**a**). The blue curve is the spin-down projection, and the red is spin up. Four peaks with different intensities are seen in each MDC, suggesting strong polarization. **c** Polarization of the out-of-plane projection of the spin in 4Hb-TaS<sub>2</sub>, extracted from the MDCs in (**b**). **e, f** Same as (**b, c**) for 2H-TaS<sub>2</sub>. No polarization is found in 2H-TaS<sub>2</sub>.



layer coupling leads to hybridization, and the individual layers are not spin-polarized.

The vanishing of the inter-layer coupling in 4Hb-TaS<sub>2</sub> naturally explains why we measure a large polarization in 4Hb-TaS<sub>2</sub> but it is not clear why we find no polarization in 2H-TaS<sub>2</sub>. Using the values for  $t$  ( $65 \pm 5$  meV) and  $\lambda_{soc} = \alpha \times k_F$  ( $130 \pm 15$  meV), we expect a polarization of about 90% in 2H-TaS<sub>2</sub>. Moreover, we don't find polarization even at the L-point (data taken with 55 eV photons), where inter-layer coupling is canceled due to a glide-mirror symmetry<sup>28</sup>.

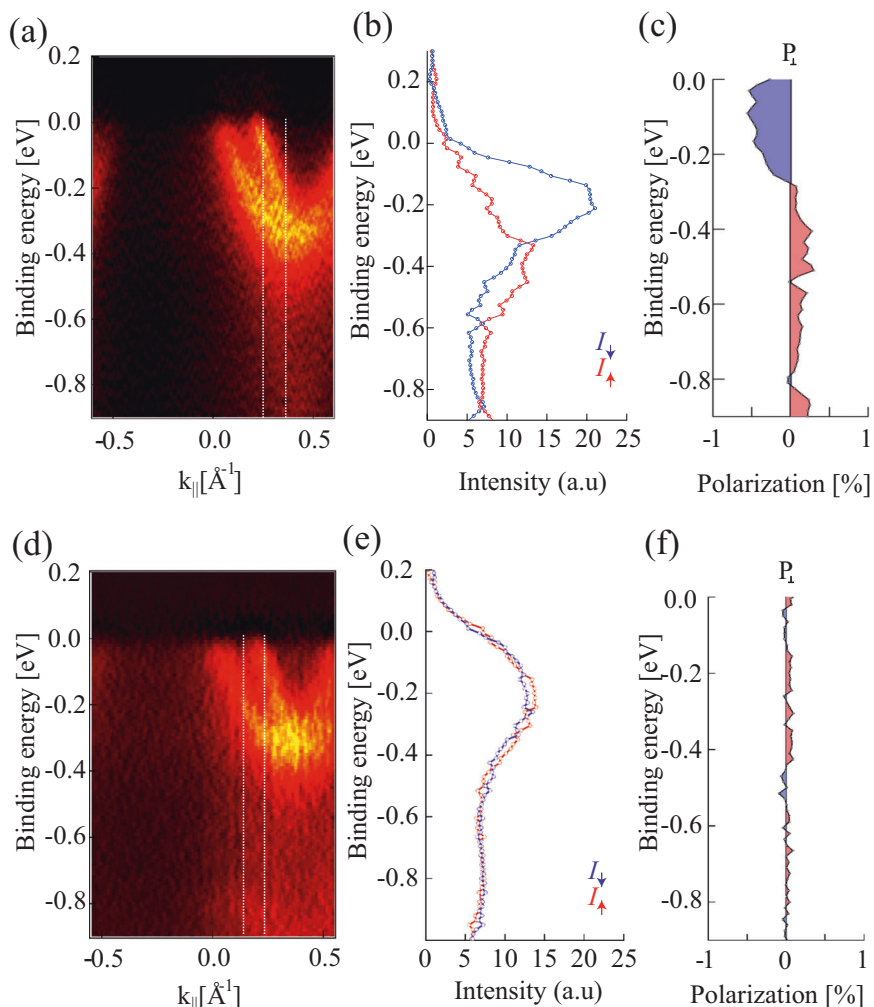
Spin-valley locking was measured using ARPES in other TMDs<sup>28,33,34</sup>. Transport measurements in a few-layers of 2H-TaS<sub>2</sub> and 2H-NbSe<sub>2</sub>, two very similar superconducting TMDs, found a smaller value of  $t/\lambda_{soc}$  in 2H-TaS<sub>2</sub><sup>27</sup>. Nevertheless, clear spin-valley locking was measured in 2H-NbSe<sub>2</sub><sup>28</sup>, but not in 2H-TaS<sub>2</sub>.

A notable difference between the two materials is the absolute value of the inter-layer coupling, which is  $\sim 32$  meV for 2H-NbSe<sub>2</sub> and  $\sim 65$  meV for 2H-TaS<sub>2</sub>. This suggests that the polarization may not be exclusively determined by  $t/\lambda_{soc}$ .

There are experimental details related to the ARPES experiment that can reduce the measured polarization in 2H-TaS<sub>2</sub> compared to 4Hb-TaS<sub>2</sub>. First, the separation between the 1H layers in 4Hb-TaS<sub>2</sub> is double than in 2H-TaS<sub>2</sub>. For a given mean-free path of the photoelectrons,  $L$ , the average polarization of the two top-most layers is given by  $\frac{1}{1+\exp(-\frac{\Delta L}{L})}$ , where  $\Delta L$  is the inter-layer distance. For a mean-free path of 8 Å, we get an average polarization of  $\sim 0.8$  for 4Hb-TaS<sub>2</sub> and  $\sim 0.6$  for 2H-TaS<sub>2</sub>.

Second, larger bandwidth normal to the planes in 2H-TaS<sub>2</sub>, combined with the finite resolution in  $k_z$ , can lead to some broadening of the ARPES

**Fig. 5 | Valley polarization.** **a, d** Band dispersion around the M-point for 4Hb-TaS<sub>2</sub> and 2H-TaS<sub>2</sub>, respectively, measured using 55 eV photons. The dashed lines show the locations of the EDCs shown in **(b, e)** respectively. **b** Spin-polarized EDCs cutting two bands in 4Hb-TaS<sub>2</sub>. The blue curve is the spin-down, and the red is spin-up, both normal to the surface. **c** Spin polarization normal to plane extracted from the EDCs in **(b)**. A polarization of nearly 70% is found for the band at low binding energies. For higher binding energies the polarization is weaker. **e, f** Same as **(b, c)** for 2H-TaS<sub>2</sub>. No polarization is found.



spectra that could mix the two spin-polarized bands. Based on the DFT calculation made for a 10-layers slab (Supplementary Note 6), we do not expect a large broadening as we move from the M-point. In addition, the spin-resolved measurement effectively improves the ability to resolve two overlapping bands.

While it seems unlikely that experimental details can mask completely a polarization of  $\sim 60\%$ , it certainly could make it more difficult to observe the polarization in 2H-TaS<sub>2</sub> compared to 4Hb-TaS<sub>2</sub>.

To summarize, we used ARPES to map the band structure of 4Hb-TaS<sub>2</sub>. Comparing the spectra of 4Hb-TaS<sub>2</sub> and 2H-TaS<sub>2</sub> we find two major differences. First, we observed a significant charge transfer from the 1T layers to the 1H layers. This charge transfer depletes almost completely the lower Hubbard band of the 1T layers, suggesting that the localized charges on the star-of-David cells that govern the physics of bulk 1T-TaS<sub>2</sub>, play a much smaller role in the physics of 4Hb-TaS<sub>2</sub>. However, we do find new small shallow pockets around the  $\Gamma$ -point. DFT shows that these new states reside mainly on the 1T-layers. The connection of these states with the unusual properties of 4Hb-TaS<sub>2</sub> is still not clear.

In addition, we find that the inter-layer coupling between 1H-layers in 4Hb-TaS<sub>2</sub> is effectively zero. This leads to strong spin-valley locking that is completely missing in bulk 2H-TaS<sub>2</sub>. The measured spin-texture can explain the Ising-superconductivity found in 4Hb-TaS<sub>2</sub> and may play a significant role in determining the superconducting order-parameter.

We provide a full detailed description of the electronic structure of 4Hb-TaS<sub>2</sub>, it remains to understand how the unusual superconducting state emerges from this electronic structure.

## Methods

### Samples growth

High quality single crystals of 2H-TaS<sub>2</sub> and 4Hb-TaS<sub>2</sub> were grown using the chemical vapor transport method, as described in refs. 7,11. Single crystals were grown using iodine as a transport agent in a sealed quartz, using a 3-zone furnace. The crystals have typical lateral size of a few mm and a thickness of about 0.5 mm. The samples are characterized by XRD, TEM, EDS and magnetization measurements (Supplementary Figs. 8 and 9). Se in 4Hb crystals is used to stabilize the 4Hb phase and improve the properties of the superconducting phase. EDS measurements show that the actual amount of Se in the crystals is on the order of 0.2% (Supplementary Note 8). The composition of the sample used in this study is 4Hb-TaS<sub>2-x</sub>Se<sub>x</sub>,  $x \sim 0.004$ .

### Angle and spin-resolved PES

High resolution ARPES was done at the Ultra end-station at the SIS beamline at PSI, Switzerland. Angle- and spin-resolved PES were performed at the RGLB-II beamline in BESSYII Berlin, Germany and the APE-LE beamline in Elettra, Italy. The light used at BESSYII beamline is p polarized, while the light used at APE-LE is s polarized. Samples were cleaved in-situ and measured at temperatures ranging from 10 to 30 K. For the spin-resolved measurements, a VLEED detector was used in APE-LE, and Mott detectors at BESSYII. A Sherman function of  $S = 0.33$  was used to generate the measured spin polarization for the data from APE-LE, and  $S = 0.16$  for the data from BESSYII.

The bands polarization is given by<sup>28,33,34</sup>:

$$P = \frac{I_{\uparrow} - I_{\downarrow}}{SI_{\uparrow} + I_{\downarrow}} \quad (2)$$

where  $P$  is the polarization measured and  $I_{\uparrow}/I_{\downarrow}$  is the measured intensity for each projection corrected by a relative detector efficiency calibration.

To determine the  $k_z$  dispersion from photon-energy-dependent ARPES, we use the free electron final state approximation for normal emission<sup>33,39–41</sup>:

$$k_z = \sqrt{2m\hbar^2(E_{kin} + V_0)} \quad (3)$$

where  $V_0$  is the inner potential and  $E_{kin}$  is the kinetic energy of the photoemitted electron. Our photon energy range covers two complete Brillouin zones along  $k_z$ . Fitting the photon energies of the Brillouin zones center ( $\Gamma$ ) and edge ( $Z$ ) gives best agreement taking an inner potential of 9 eV. We use the same inner potential for both 2H-TaS<sub>2</sub> and 4Hb-TaS<sub>2</sub>.

### Density-functional theory

We performed density-functional theory (DFT) calculations using the generalized gradient approximation (GGA) in the Perdew–Burke–Ernzerhof (PBE) form with the Vienna ab initio package<sup>42</sup>.

The DFT-D2 method was used to account for van der Waals (vdW) interactions<sup>43</sup>.

Spin-orbit coupling (SOC) was included in all calculations. We employ a  $\sqrt{13} \times \sqrt{13} \times 1$  supercell as an initial approach to describe the CDW phase of 4Hb-TaS<sub>2</sub>.

To simulate the properties of 4Hb-TaS<sub>2</sub> in a computationally efficient manner, we simplify the system by considering a bi-layer configuration of 1T-TaS<sub>2</sub> and 1H-TaS<sub>2</sub>. These polytypes have been chosen to maintain the essential characteristics of the 4Hb phase.

The effective band structures (EBS) method in VASPKIT<sup>44</sup> was used to directly compare with experimental measurements by unfolding the band structures of supercells into the Brillouin zone of primitive unit cells.

To explore the surface states of 2H and 4Hb surfaces, we used 10-unitcell thick slab models and projected bands to the H layer as the surface bands. Because we were interested in the H layer bands, we ignored the CDW distortion in the 1T layer in the 4Hb slab model use a  $1 \times 1$  unit cell in the basal plane.

### Data availability

The data that support the findings of this study are provided in the main text and the Supplementary Information. The original data is available from the corresponding author upon request.

Received: 25 October 2023; Accepted: 2 April 2024;

Published online: 10 April 2024

### References

- Novoselov, K. S., Mishchenko, A., Carvalho, A. & Castro Neto, A. 2D Materials and van der Waals heterostructures. *Science* **353**, aac9439 (2016).
- Cao, Y. et al. Unconventional superconductivity in magic-angle graphene superlattices. *Nature* **556**, 43 (2018).
- Cao, Y. et al. Correlated insulator behaviour at half-filling in magic-angle graphene superlattices. *Nature* **556**, 80 (2018).
- Vizner Stern, M. et al. Interfacial ferroelectricity by van der Waals sliding. *Science* **372**, 1462 (2021).
- Cao, Y. et al. Nematicity and competing orders in superconducting magic-angle graphene. *Science* **372**, 264 (2021).
- Chen, G. et al. Tunable correlated Chern insulator and ferromagnetism in a moiré superlattice. *Nature* **579**, 56 (2020).
- Di Salvo, F., Bagley, B., Voorhoeve, J. & Waszczak, J. Preparation and properties of a new polytype of tantalum disulfide (4Hb-TaS<sub>2</sub>). *J. Phys. Chem. Solids* **34**, 1357 (1973).
- Ribak, A. et al. Gapless excitations in the ground state of 1T-TaS<sub>2</sub>. *Phys. Rev. B* **96**, 195131 (2017).
- Nayak, A. K. et al. Evidence of topological boundary modes with topological nodal-point superconductivity. *Nat. Phys.* **17**, 12 (2021).
- Persky, E. et al. Magnetic memory and spontaneous vortices in a van der Waals superconductor. *Nature* **607**, 692 (2022).
- Ribak, A. et al. Chiral superconductivity in the alternate stacking compound 4Hb-TaS<sub>2</sub>. *Sci. Adv.* **6**, eaax9480 (2020).
- Almoalem, A. et al. Evidence of a two-component order parameter in 4Hb-TaS<sub>2</sub> in the little parks effect. Preprint at <https://arxiv.org/abs/2208.13798> (2023).
- Vavno, V. et al. Artificial heavy fermions in a van der Waals heterostructure. *Nature* **599**, 582 (2021).
- Crippa, L. et al. Heterogeneous Ta-dichalcogenide bilayer: heavy fermions or doped Mott physics? Preprint at <https://arxiv.org/abs/2302.14072> (2023).
- Law, K. T. & Lee, P. A. 1T-TaS<sub>2</sub> as a quantum spin liquid. *Proc. Natl. Acad. Sci. USA* **114**, 6996 (2017).
- Liu, C., Chatterjee, S., Scaffidi, T., Berg, E. & Altman, E. Magnetization amplification in the interlayer pairing superconductor 4Hb-TaS<sub>2</sub>. Preprint at <https://arxiv.org/abs/2307.10389> (2023).
- König, E. J. Type-II heavy Fermi liquids and the magnetic memory of 4Hb-TaS<sub>2</sub>. *Phys. Rev. Res.* **6**, L012058 (2024).
- Kim, J.-J. & Olin, H. Atomic and electronic structure study on the layers of 4Hb-TaS<sub>2</sub> prepared by a layer-by-layer etching technique. *Phys. Rev. B* **52**, R14388 (1995).
- Goryo, J., Fischer, M. H. & Sigrist, M. Possible pairing symmetries in SrPtAs with a local lack of inversion center. *Phys. Rev. B* **86**, 100507 (2012).
- Lahoud, E., Meetei, O. N., Chaska, K., Kanigel, A. & Trivedi, N. Emergence of a novel pseudogap metallic state in a disordered 2D Mott insulator. *Phys. Rev. Lett.* **112**, 206402 (2014).
- Yang, H. F. et al. Visualization of chiral electronic structure and anomalous optical response in a material with chiral charge density waves. *Phys. Rev. Lett.* **129**, 156401 (2022).
- Nayak, A. K. et al. First-order quantum phase transition in the hybrid metal–Mott insulator transition metal dichalcogenide 4Hb-TaS<sub>2</sub>. *Proc. Natl. Acad. Sci. USA* **120**, e2304274120 (2023).
- Shen, S. et al. Coexistence of Quasi-two-dimensional superconductivity and tunable Kondo lattice in a van der Waals superconductor. *Chinese Phys. Lett.* **39**, 077401 (2022).
- Sanders, C. E. et al. Crystalline and electronic structure of single-layer TaS<sub>2</sub>. *Phys. Rev. B* **94**, 081404 (2016).
- Xiao, D., Liu, G.-B., Feng, W., Xu, X. & Yao, W. Coupled spin and valley physics in monolayers of and other group-VI dichalcogenides. *Phys. Rev. Lett.* **108**, 196802 (2012).
- Yang, Y. et al. Enhanced superconductivity upon weakening of charge density wave transport in 2H-TaS<sub>2</sub> in the two-dimensional limit. *Phys. Rev. B* **98**, 035203 (2018).
- De la Barrera, S. C. et al. Tuning Ising superconductivity with layer and spin–orbit coupling in two-dimensional transition-metal dichalcogenides. *Nat. Commun.* **9**, 1427 (2018).
- Bawden, L. et al. Spin–valley locking in the normal state of a transition-metal dichalcogenide superconductor. *Nat. Commun.* **7**, 1 (2016).
- Dentelski, D., Day-Roberts, E., Birol, T., Fernandes, R. M. & Ruhman, J. Robust gapless superconductivity in 4Hb-TaS<sub>2</sub>. *Phys. Rev. B* **103**, 224522 (2021).
- Gong, Z. et al. Magnetoelectric effects and valley-controlled spin quantum gates in transition metal dichalcogenide bilayers. *Nat. Commun.* **4**, 2053 (2013).
- Ritschel, T. et al. Orbital textures and charge density waves in transition metal dichalcogenides. *Nat. Phys.* **11**, 328 (2015).

32. Zhang, X., Liu, Q., Luo, J.-W., Freeman, A. J. & Zunger, A. Hidden spin polarization in inversion-symmetric bulk crystals. *Nat. Phys.* **10**, 387 (2014).
33. Riley, J. M. et al. Direct observation of spin-polarized bulk bands in an inversion-symmetric semiconductor. *Nat. Phys.* **10**, 835 (2014).
34. Razzoli, E. et al. Selective Probing of hidden spin-polarized states in inversion-symmetric bulk MoS<sub>2</sub>. *Phys. Rev. Lett.* **118**, 086402 (2017).
35. Xie, L. & Cui, X. Manipulating spin-polarized photocurrents in 2D transition metal dichalcogenides. *Proc. Natl. Acad. Sci. USA* **113**, 3746 (2016).
36. Roch, J. G. et al. Spin-polarized electrons in monolayer MoS<sub>2</sub>. *Nat. Nanotechnol.* **14**, 432 (2019).
37. Huang, Y. et al. Hidden spin polarization in the centrosymmetric MoS<sub>2</sub> crystal revealed via elliptically polarized terahertz emission. *Phys. Rev. B* **102**, 085205 (2020).
38. Lawson, B. J. et al. Quantum oscillations in Cu<sub>x</sub>Bi<sub>2</sub>Se<sub>3</sub> in high magnetic fields. *Phys. Rev. B* **90**, 195141 (2014).
39. Damascelli, A., Hussain, Z. & Shen, Z.-X. Angle-resolved photoemission studies of the cuprate superconductors. *Rev. Modern Phys.* **75**, 473 (2003).
40. Lahoud, E. et al. Evolution of the Fermi surface of a doped topological insulator with carrier concentration. *Phys. Rev. B* **88**, 195107 (2013).
41. Almoalem, A. et al. Link between superconductivity and a Lifshitz transition in intercalated Bi<sub>2</sub>Se<sub>3</sub>. *Phys. Rev. B* **103**, 174518 (2021).
42. Kresse, G. & Joubert, D. From ultrasoft pseudopotentials to the projector augmented-wave method. *Phys. Rev. B* **59**, 1758 (1999).
43. Grimme, S. Semiempirical GGA-type density functional constructed with a long-range dispersion correction. *J. Comput. Chem.* **27**, 1787 (2006).
44. Wang, V., Xu, N., Liu, J.-C., Tang, G. & Geng, W.-T. VASPKIT: a user-friendly interface facilitating high-throughput computing and analysis using VASP code. *Comput. Phys. Commun.* **267**, 108033 (2021).

## Acknowledgements

We acknowledge the Paul Scherrer Institute, Villigen, Switzerland for provision of synchrotron radiation beamtime at beamline SIS of the SLS. We acknowledge Elettra Synchrotron, Trieste for providing access to its synchrotron radiation facilities. We thank the Helmholtz-Zentrum, Berlin for the allocation of synchrotron radiation beamtime. The work at the Technion was supported by Israeli Science Foundation grant number ISF-1263/21. This work has been partly performed in the framework of the nanoscience foundry and fine analysis (NFFA-MUR Italy Progetti Internazionali) facility.

## Author contributions

A.K. conceived the project. A.A. performed the ARPES measurements and analyzed the data. R.G, Y.N., and I.M. helped with ARPES measurements. I.F. synthesized the single crystals. J.K. performed DFT calculations. F.M., I.V., J.F., J.S.B, O.J.C., N.C.P., and M.S. provided support at the synchrotron beam-lines. B.Y. supervised the DFT calculations and performed theoretical modeling. A.A. and A.K. wrote the manuscript with contributions from all authors.

## Competing interests

The authors declare no competing interests.

## Additional information

**Supplementary information** The online version contains supplementary material available at <https://doi.org/10.1038/s41535-024-00646-2>.

**Correspondence** and requests for materials should be addressed to Amit Kanigel.

**Reprints and permissions information** is available at <http://www.nature.com/reprints>

**Publisher's note** Springer Nature remains neutral with regard to jurisdictional claims in published maps and institutional affiliations.

**Open Access** This article is licensed under a Creative Commons Attribution 4.0 International License, which permits use, sharing, adaptation, distribution and reproduction in any medium or format, as long as you give appropriate credit to the original author(s) and the source, provide a link to the Creative Commons licence, and indicate if changes were made. The images or other third party material in this article are included in the article's Creative Commons licence, unless indicated otherwise in a credit line to the material. If material is not included in the article's Creative Commons licence and your intended use is not permitted by statutory regulation or exceeds the permitted use, you will need to obtain permission directly from the copyright holder. To view a copy of this licence, visit <http://creativecommons.org/licenses/by/4.0/>.

© The Author(s) 2024